Liquid phase dehydration of 1-indanol: Selective synthesis of indene over microporous acid catalysts

Nicolás M. Bertero, Germán D. Bustos, Cristián A. Ferretti, Carlos R. Apesteguía, Alberto J. Marchi[*]

Catalysis Science and Engineering Research Group (GICIC), Instituto de Investigaciones en Catálisis y Petroquímica (INCAPE), UNL-CONICET, Santiago del Estero 2654, 3000 Santa Fe, Argentina

ARTICLE INFO

ABSTRACT

The selective dehydration of 1-indanol in liquid-phase was studied at 363 K and 2 bar, over solid acid catalysts, and using cyclohexane as a solvent. Mesoporous $SiO_2-Al_2O_3$ with a high density of strong Lewis acid sites produced di-1-indanyl ether and other heavy products apart from indene. In contrast, the overall selectivity to indene with beta zeolite (HBEA, Si/Al = 12.5), HZSM-5 (Si/Al = 20) and deal-uminated mordenite zeolite (HMOR, Si/Al = 80) was almost 100%. The transition state shape selectivity and a moderate density of both Lewis and Brønsted acid sites were crucial to achieve high selectivity to indene. In spite of the high overall selectivity, the final yield in indene with HBEA was only 55%. This was attributed to the formation of heavy compounds inside the large cavities of HBEA, which cannot diffuse through its micropores. In contrast, yields in indene higher than 90% were obtained with HMOR and HZSM-5. It was also observed that the yield in indene increased with time even after reaching the 1-indanol total conversion, which indicates the slow diffusion of the reactant and product molecules inside of the microporous network of HMOR and HZSM-5. Therefore, a process involving liquid phase dehydration of 1-indanol, employing one of these two zeolites as a catalyst would provide: 1) high yield in indene; 2) easy separation of product from solvent; 3) easy separation of the catalyst from the reaction medium.

© 2015 Elsevier Inc. All rights reserved.

1. Introduction

Indene (benzocyclopenta-1,3-diene) is a key intermediate in Fine Chemistry for the synthesis of pharmaceuticals [1,2], resins [3,4], metal ligands for Ziegler—Natta type catalysts [5,6] and functional materials [7]. This valuable chemical is commonly obtained from three procedures: 1) separation of indene from oil heavy residues (coal tar); 2) gas-phase conversion of some hydrocarbons at high temperature; 3) liquid-phase synthesis using mild conditions.

The traditional processes, based on the recovery from coal tar, need several complex unit operations to separate the indene from other components with similar volatility [8—12]. The most common impurities in the indene-rich streams are benzonitrile, indane, alquilbenzenes, phenols, pyridines and anilines that must be removed by alkaline or acid washings, fractional distillation, crystallization at very low temperature, and/or azeotropic distillation [10—12].

On the other hand, gas-phase reactions for indene production are carried out at high temperature in flow or fluidized bed reactors [13—22]. The most common gas-phase processes are: dehydrogenation of indane [13,14] and tetrahydroindene [14—17], dehydrocyclization of alkylbenzenes [18,19], cyclization of allylbenzene [20], and one-pot hydrogenation/dehydration feeding 1-indanone [21,22]. The main drawbacks of these gas-phase processes are: 1) low indene yields, 2) catalyst deactivation, 3) high energy consumption to volatilize the liquid reactants, and 4) the use of benzene, which is very toxic, carcinogenic, and polluting.

There are very few reports dealing with the production of indene in liquid phase. Kuch and Herrington patented a process based on the coupling between benzene and propylene at 473 K, followed by cyclization, using gold complexes as catalysts and

benzene as reactant and solvent [23]. The final indene yield, at 75% propylene conversion, was lower than 20% due to the formation of styrene and methylstyrene. This process shows the following drawbacks: a) the use of expensive catalysts; b) the low yield and selectivity to indene; c) the use of large amounts of benzene.

Taking into account all the issues mentioned above, it is concluded that it is necessary to develop a new successful and eco-friendly method to obtain a high yield in indene. One alternative could be the one-pot hydrogenation/dehydration tandem in liquid phase, starting from the corresponding ketone [24]. In a previous work, we reported the selective hydrogenation of 1-indanone to 1-indanol in liquid phase over Cu-based catalysts [25]. Therefore, the catalytic dehydration of 1-indanol (NOL) appears as a potential second step of a one-pot process in liquid phase to obtain indene (ENE) from 1-indanone.

Depending on the acid properties of the catalyst and the experimental conditions, NOL can be dehydrated following either an intramolecular or an intermolecular mechanism. The intramolecular dehydration is preferable since it leads to the target olefin, while the intermolecular mechanism produces di-1-indanyl ether (ETH), as shown in Scheme 1. Both ENE and ETH, primary products, can be subsequently converted to undesirable heavy products (HP), such as 2-(2′3′-dihydro-1′H-inden-1′-yl)-1H-indene and 6-(2′,3′-dihydro-1′H-inden-1′-yl)-1H-indene (Scheme 1). To our knowledge, there are few works dealing with the 1-indanol dehydration in liquid-phase. For example, Tarlani et al. [26] and E. Alesso et al. [27] found that unsupported heteropolyacids catalysts were selective to the intramolecular dehydration of NOL into ENE. However, a consecutive and fast HP formation was observed on this type of catalysts and, as a consequence, a yield in indene of only 25% after 20 min was reached due to the formation of 2-(2′,3′-dihydro-1′H-inden-1′-yl)-1H-indene.

In this work, the liquid-phase dehydration of 1-indanol was studied over different silicoaluminates. The aim of this work is to determine the feasibility of carrying out a selective liquid phase dehydration of 1-indanol at low temperatures through an intramolecular mechanism and to inhibit the subsequent conversion of the primary alkene into heavy products. This intramolecular dehydration step could be coupled with the selective hydrogenation of 1-indanone to 1-indanol in order to develop an eco-friendly one-pot process in liquid phase to produce indene.

2. Experimental

2.1. Sample preconditioning

Commercial samples of SiO_2–Al_2O_3 (Ketjen LALPV) and zeolites HZSM-5 (Zeocat Pentasil PZ-2/54), dealuminated mordenite (HMOR, Zeocat HZM-980) and beta (HBEA, Zeocat PB) were calcined in air flow (60 cm^3/min) at 773 K for 2 h before performing any characterization or catalytic test.

2.2. Characterization

The polycrystalline species in the calcined samples were identified by X-ray diffraction (XRD) using a Shimadzu XD-1 diffractometer and Ni-filtered Cu-Kα radiation (scan speed 2°/min). The textural properties of the solid acids were determined by N_2 physisorption at 77 K in a Quantochrome Corporation NOVA-1000 sorptometer. Specific surface area (S_{BET}) was determined by applying the BET equation, following the criteria of Parra et al. [28,29]. Zeolite micropore volumes were determined by the t-plot [30] method, using Harkins–Jura equation [31]. For SiO_2–Al_2O_3, the pore volume (V_P) and pore mean diameter were estimated by Barrett–Joyner–Halenda (BJH) method. The elemental compositions were determined by atomic absorption spectroscopy (AAS).

The density and relative strength of acid sites were determined by temperature-programmed desorption (TPD) of NH_3 preadsorbed at 373 K. Previously calcined samples (200 mg) were treated in He (60 cm^3/min) at 773 K for 0.5 h, cooled down to 373 K, and then exposed to a 1% NH_3/He stream for 45 min. Weakly adsorbed NH_3 was removed by flushing with He at 373 K during 2 h. Finally, the temperature was increased at 10 K/min and the NH_3 concentration in the effluent was followed by mass spectrometry (MS) in a Baltzers Omnistar unit.

The surface Lewis/Brønsted balance was determined by Fourier transform infrared spectroscopy (FTIR), using pyridine as a probe molecule and a Shimadzu FTIR-8101M spectrophotometer. Sample wafers were formed by pressing 20–40 mg of the solids at 5 ton/cm^2 and then were transferred to a quartz sample holder. An inverted T-shaped Pyrex cell containing the sample pellet was used for the measurements. The calcined sample was placed in the cell and then outgassed at 723 K for 4 h. A background spectrum was recorded after cooling the sample at room temperature. The data were obtained after the admission of pyridine, adsorption at room temperature, and evacuation at 423 K for 0.5 h. The absorbance scale was normalized to 1-g samples and the spectra were recorded at room temperature.

2.3. Catalytic tests

The dehydration of NOL was carried out in liquid phase, using a 600 ml mechanically stirred autoclave (Parr 4843). The initial concentration of NOL was 0.08 M and the reaction temperature was set at 363 K. After charging to the autoclave 150 ml of solvent
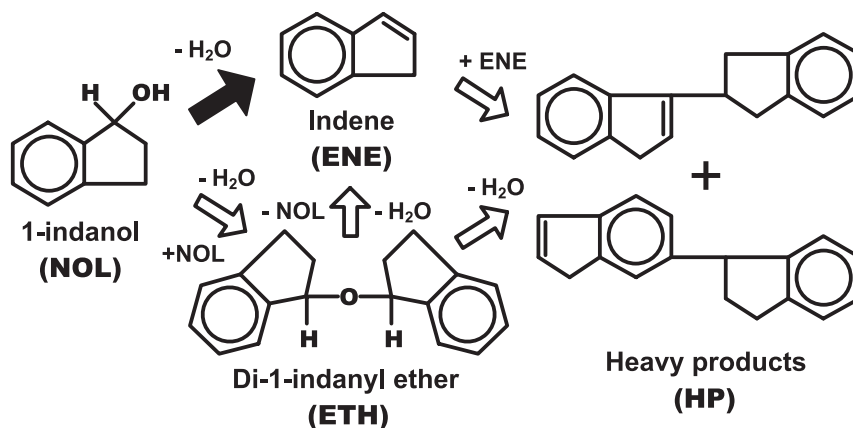
Scheme 1. Reaction network for 1-indanol dehydration over acid catalysts.

(cyclohexane 99%, Merck) and 0.25 g of catalyst, previously calcined ex-situ in 60 cm^3/min air flow at 773 K for 2 h, the stirring was started under inert N$_2$ atmosphere and the autoclave was heated up to 363 K. Afterwards, 1.68 g of NOL (1-indanol 99%, Aldrich) was injected to the reactor to start the reaction and the system pressure was set at 2 bar with N$_2$. Stirring speed was 600 RPM and the particle diameters were smaller than 100 μm [32]. Liquid samples were collected from the reactor every 5–30 min. A pressurized loop was used to avoid flash evaporation of samples. Using this loop, only less than a 3% of the total liquid volume was extracted during the run.

The concentrations of the unreacted NOL and the reaction products were monitored during the reaction by ex-situ gas chromatography using an Agilent 6850 chromatograph equipped with a flame ionization detector at 523 K, a temperature programmer, and a 50 m HP-1 capillary column with a 1.05 μm coating. The reactant conversion (X_{NOL}, mol of NOL reacted/mol of NOL fed) was calculated as $X_{NOL} = (C^0_{NOL} - C_{NOL})/C^0_{NOL}$, where C^0_{NOL} is the initial NOL concentration in liquid phase and C_{NOL} is the NOL concentration in liquid phase at reaction time t. Yields (η_j, mol of product j/mol of NOL fed) were calculated as $\eta_j = C_j/C^0_{NOL}$, where C_j is the concentration of product j in liquid phase. Three definitions of selectivity were considered in this work: a) initial selectivity to ENE (S^0_{ENE}) calculated as $S^0_{ENE} = 100 \cdot r^0_{ENE}/(r^0_{ENE} + 2 \cdot r^0_{ETH})$, taking into account the stoichiometry of the primary reactions, where r^0_i is the initial formation rate of product i, which was calculated by differentiation of a second grade polynomial obtained by numerical regression [32]; b) overall selectivity (S_j, mol of product j in liquid phase/mol of products in liquid phase) calculated as $S_j = 100 \cdot C_j/\Sigma C_j$, where C_j is the concentration of product j in liquid phase; c) local selectivity (S'_j, mol of product j in liquid phase/mol of NOL converted) calculated as $S'_j = 100 \cdot \eta_j/X_{NOL}$. Finally, the carbon balance, at a given reaction time t, was checked by applying the following equation:

$$\%C = 100 \cdot (C_{NOL} + C_{ENE} + 2 \cdot C_{ETH} + 2 \cdot C_{HP}) \big/ C^0_{NOL}.$$

2.4. Molecular modeling

Molecular orbital calculations within the Density Functional Theory (DFT) formalism were performed using the gradient corrected Becke's three parameters hybrid exchange functional in combination with the correlation functional of Lee, Yang and Parr (B3LYP) [33]. All the calculations were carried out using the Gaussian-03 program package [34]. The molecular orbitals of molecules were described with the 6-31G(d,p) basis set. Critical diameters (CD) were considered as the internuclear distance between the two nuclei that intersects the surface of the smallest possible cylinder containing all nuclei plus an estimate of the Van der Waals radii of the hydrogen (1.2 Å) or oxygen (1.5 Å) atoms implicated; and molecules critical lengths (CL) were computed as the distance between the two farthest atoms along a line orthogonal to the critical diameter, plus an estimate of the atoms radii.

The kinetic diameters of the reactant and product molecules were estimated using correlations based on the molecular weight and properties at the critical point [35,36].

3. Results and discussion

3.1. Catalyst characterization

XRD was performed firstly to determine qualitatively the influence of calcination in dry air flow at 773 K on the zeolite crystalline structure. The X-ray diffractograms obtained for calcined

HBEA, HZSM-5 and HMOR zeolites (Fig. 1) were similar to the patterns reported in literature, which indicates that the crystalline structure of the samples was preserved after calcination. In the case of SiO$_2$–Al$_2$O$_3$, only the characteristic amorphous halo [37] was observed (not shown here).

The textural properties and the Si/Al ratio of the calcined samples are presented in Table 1. It can be observed that the four solids have a relatively large specific surface area ($S_{BET} \geq 350$ m^2/g). The specific surface areas of HMOR and HBEA are larger than those determined for HZSM-5 and mesoporous SiO$_2$–Al$_2$O$_3$. However, the pore volume (V_P) of SiO$_2$–Al$_2$O$_3$, determined by BJH method, is between two and four times those of zeolites, determined by t-plot method (Table 1). In the case of zeolites, the pattern for specific surface area and pore volume was: HZSM-5 < HBEA < HMOR. In particular, SiO$_2$–Al$_2$O$_3$ showed an intermediate specific surface area but the largest pore volume of the series.

Density and relative strength of acid sites for the calcined samples were probed by TPD of NH$_3$ preadsorbed at 373 K (Fig. 2). The amounts of desorbed NH$_3$ per gram of sample and per square meter, considered as a measure of the acid site density, were determined by deconvolution and integration of these NH$_3$-TPD curves (Table 2). The resulting values showed that the acid sites density of the samples, both per gram of catalyst and per square meter of specific surface area, followed the pattern: SiO$_2$–Al$_2$O$_3 \geq$ HZSM-5 > HBEA > HMOR. A very broad and asymmetric desorption band between 423 and 873 K, with a maximum at 483–493 K, was observed for SiO$_2$–Al$_2$O$_3$ (Fig. 2). This reflects a wide range of acidity for the surface acid sites on this sample. Besides, NH$_3$ desorption rate diminished as the acid site strength increased. HBEA exhibited a similar asymmetric desorption band but between 373 and 773 K, with a maximum at 500 K, approximately. No NH$_3$ desorption at $T > 773$ K was detected, which reveals the absence of very strong acid sites on the HBEA surface. This NH$_3$-TPD profile is qualitatively similar to those previously reported for zeolites HBEA with similar Si/Al ratio [38]. In contrast, two overlapping but well-distinguished NH$_3$ desorption bands were observed with HZSM-5: one between 403 and 633 K and another one between 583 and 863 K, which shows the presence of both weak and strong acid sites. Finally, two well-differentiated NH$_3$ desorption peaks were detected for HMOR: one between 400 and 550 K, corresponding to weak acid sites, and another one between 593 and 873 K, which reflects the presence of strong acid sites, in agreement with results reported in a previous work [39].
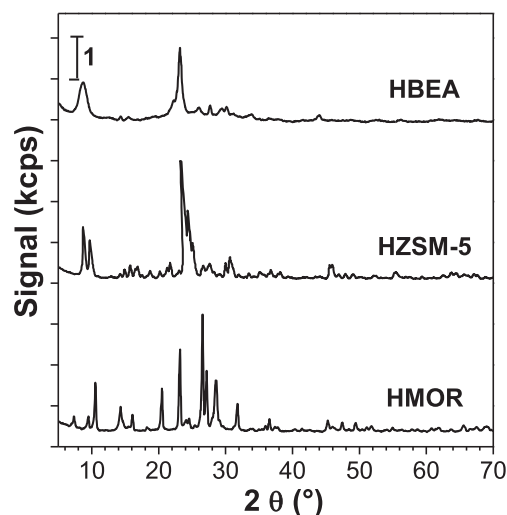

Fig. 1. X-ray diffractograms of calcined zeolite samples.

Table 1
Textural properties of the samples.

Sample	Topology[a]	Si/Al[b]	S_{BET} (m^2/g)[c]	V_P (cm^3/g)	Channel dimensions (Å)
SiO$_2$–Al$_2$O$_3$	–	11.2	455	0.74[d]	50[d]
HBEA	BEA	12.5	560	0.17[e]	6.6 × 6.7; 5.6 × 5.6[f]
HZSM-5	MFI	20	350	0.16[e]	5.1 × 5.5; 5.3 × 5.6
HMOR	MOR	80	650	0.30[e]	6.5 × 7.0; 3.4 × 4.8; 2.6 × 5.7

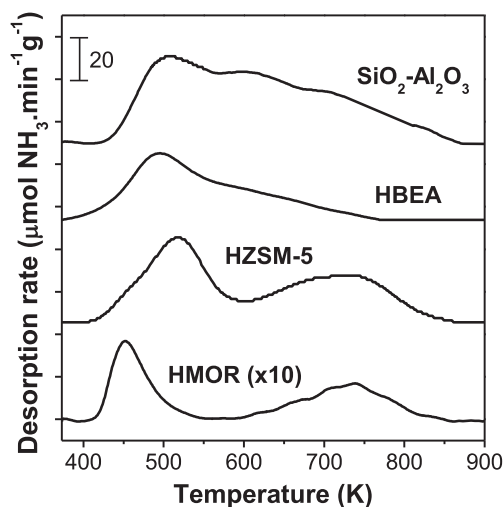[a] From the International Zeolite Association [56].
[b] Si/Al molar ratio determined by AAS.
[c] Determined by BET method [28,29].
[d] Determined by BJH method.
[e] Micropore volume determined by *t*-plot method.
[f] Channel intersections of HBEA zeolite generate cavities of about 12 Å [51,52].

Fig. 2. NH$_3$-TPD profiles for the calcined samples.

Similar patterns were observed for the total density of surface acid sites and the concentration of strong acid sites obtained from the NH$_3$ desorbed at $T > 523$ K: SiO$_2$–Al$_2$O$_3$ > HZSM-5 > HBEA > HMOR (Table 2). The ratio of strong to weak acid sites showed the following trend: SiO$_2$–Al$_2$O$_3$ > HZSM-5 > HMOR ≅ HBEA.

The nature of surface acid sites was determined by FTIR of pyridine adsorbed on the calcined samples. The FTIR spectra obtained, in the range 1400–1700 cm^{-1}, are shown in Fig. 3. The pyridine adsorption bands at around 1540 cm^{-1} and 1440–1460 cm^{-1} arise from pyridine adsorbed on Brønsted (B) and Lewis (L) sites, respectively [40]. The relative contributions of Lewis and Brønsted acid sites were obtained by deconvolution and numerical integration of pyridine absorption bands at around 1450 and 1540 cm^{-1}, followed by correction with extinction coefficients determined from the infrared absorption bands of pyridine

adsorbed on zeolites and amorphous silica-alúminas [41]. The results are summarized in Table 2.

It was observed that both Lewis and Brønsted acid sites are present on SiO$_2$–Al$_2$O$_3$ surface. The band at 1455 cm^{-1} reflects the adsorption of pyridine through a dative bond on Lewis acid sites associated with tricoordinate Al atoms [42]. The band at 1543–1545 cm^{-1} reveals the adsorption of pyridine on Brønsted acid sites. From the numerical integration of these two bands and applying the corresponding extinction coefficients, a relationship between Lewis and total acid sites L/(L + B) of 0.71 was estimated. On HBEA, the IR bands attributed to pyridine adsorbed on Brønsted and Lewis acid sites appeared at 1542 and 1455 cm^{-1}, respectively. In this case, the L/(L + B) ratio was 0.48, which indicates that surface density of L and B acid sites is similar (Table 2). On HZSM-5, the 1440–1460 cm^{-1} band was split in two overlapping peaks corresponding to pyridine adsorbed on Al (band at 1450 cm^{-1}) and Na (band at 1445 cm^{-1}) Lewis acid sites [32]. An infrared band at 1542 cm^{-1}, due to pyridine adsorbed on Brønsted acid sites, was also observed. In this case, the relative concentration of Brønsted and Lewis surface acid sites on HZSM-5 surface was similar to that estimated for HBEA, i.e. L/(L + B) = 0.45 (Table 2). HMOR also showed both Lewis and Brønsted pyridine adsorption bands at 1453 and 1544 cm^{-1}, respectively [39]. However, the lowest L/(L + B) ratio of the series, L/(L + B) = 0.1, was obtained from these two bands (Table 2). In summary, the ratio of Lewis to Brønsted sites on the sample surfaces followed the pattern: SiO$_2$–Al$_2$O$_3$ > HBEA ≅ HZSM-5 > HMOR. It is worth to notice that, at least in the case of zeolites, the total acid site density obtained from FTIR of adsorbed pyridine on L and B surface acid sites is quite similar to the acid site density determined from NH$_3$ desorbed at $T > 523$ K (Table 2).

3.2. Catalytic tests

The NOL conversion (X_{NOL}) as a function of time is represented for each catalyst in Fig. 4. The four samples were active in the NOL dehydration and reached at least $X_{NOL} = 90\%$ in less than 2 h under

Table 2
Acidic properties of the samples.

| Sample	TPD of NH$_3$ Acid site density				FTIR of pyridine Acid site nature			
	Total NH$_3$ desorbed		$T > 523$ K		B[a]	L[b]	B + L	L/(L + B)
	(μmol/g)	(μmol/m^2)	(μmol/g)	(μmol/m^2)	(μmol/g)	(μmol/g)	(μmol/g)	
SiO$_2$–Al$_2$O$_3$	1026	2.3	764	1.7	51	122	173	0.71
HBEA	498	0.9	261	0.5	148	136	284	0.48
HZSM-5	770	2.2	531	1.5	249	204	453	0.45
HMOR	98	0.2	52	0.1	46	5	50	0.10

[a] Brønsted sites concentration obtained from the FTIR band at 1540 cm^{-1} of adsorbed pyridine.
[b] Lewis sites concentration obtained from the FTIR band at 1440–1460 cm^{-1} of adsorbed pyridine.
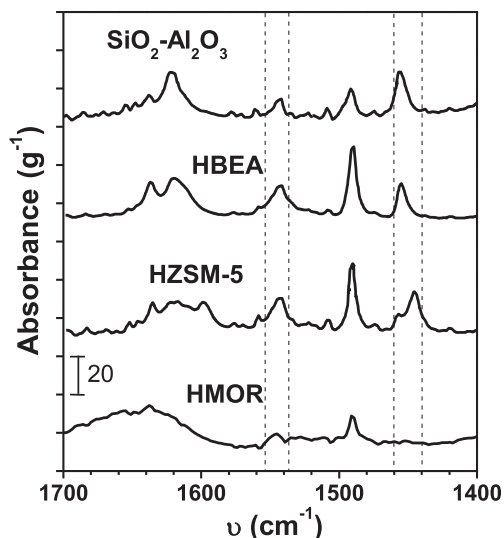
Fig. 3. FTIR spectra of pyridine adsorbed at 298 K on calcined samples and outgassed at 423 K.

the conditions described in this work. The initial NOL conversion rates, r^0_{NOL} (mol·g^{-1}·min^{-1}), were calculated from these X_{NOL} vs. time experimental data by applying numerical polynomial regression and subsequent differentiation at zero time. The r^0_{NOL} values obtained are summarized in Table 3. From these results, the following pattern for the initial activity was obtained: HBEA > HMOR > SiO$_2$–Al$_2$O$_3$ > HZMS-5. The reaction times to reach a NOL conversion of 50 and 90% are also presented in Table 3. It was determined that the catalytic activity pattern at high NOL conversion was the same as the one observed for the initial activity. In general, the activity pattern for NOL dehydration in liquid phase (Table 3) did not match with the acid site density patterns obtained from NH$_3$-TPD (Table 2). For example, HBEA, with an intermediate acid site density, showed the highest initial activity for NOL dehydration under the experimental conditions used in this work. On the other hand, HZSM-5, with the highest acid site density of strong surface acid sites of the zeolites, was the least active catalyst of these series for dehydrating NOL. Besides, the initial NOL conversion rate with HZSM-5 ($r^0_{NOL} = 6.9 \times 10^{-4}$ mol g^{-1}·min^{-1}) is about three times lower than the value obtained in a previous
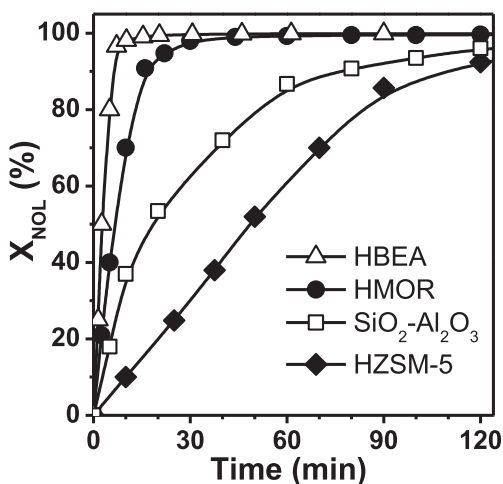
work for 1-phenylethanol (PHE) conversion rate ($r^0_{PHE} = 1.9 \times 10^{-3}$ mol g^{-1}·min^{-1}) under the same experimental conditions [32]. Both reactants, NOL and PHE, are secondary alcohols with similar molecular structures that can form carbocations of comparable stability. As a consequence, a similar reactivity for the dehydration of both NOL and PHE can be expected. However, as the kinetic diameter of NOL is larger than that of PHE, we assumed that the lower initial activity observed for NOL dehydration indicates that some restrictions for diffusion of NOL molecules inside HZSM-5 micropores affect the r^0_{NOL} value. This assumption was confirmed by calculating the intraparticle mass transfer limitations using the experimental criterion of Ramachandran and Chaudhari [43]. It is worth mentioning that no diffusion limitations were determined for SiO$_2$–Al$_2$O$_3$ by applying the same criterion.

On the other hand, the high activity observed for HMOR (Table 3), which has the lowest density of surface acid sites of this series, can be explained on the basis of a high average intrinsic activity of its surface acid sites. This is probably due to the strong surface acid sites on HMOR surface, in agreement with the high Si/Al ratio of this dealuminated zeolite (Table 2). According to previous works, as the subsequent dealumination of the synthesized mordenite unblocks the largest micropores, the strongest acid sites of HMOR become accessible for large molecules as NOL [44,39].

Average TOF values were calculated from r^0_{NOL} and r^0_{ENE} considering the total acid site density (TOF$_{NOL}$) and the concentration of surface B acid sites (TOF$_{ENE}$), both determined by FTIR of adsorbed pyridine (Table 3). In both cases, a diminution of the TOF$_{NOL}$ and TOF$_{ENE}$ with the increase of the surface acid site concentration on zeolites was observed (Tables 2 and 3). Zeolite HMOR, which has the lowest surface density of acid sites, showed the highest activity per surface acid site of the series. These TOF values explain the similar catalytic activity observed for HMOR and HBEA (Table 3 and Fig. 4), in spite of the higher total and strong acid site density of HBEA with respect to HMOR (Table 2). It is worth noticing that HMOR has surface acid sites that desorbed NH$_3$ at temperatures higher than HBEA (Fig. 2). It is likely that these strong acid sites are responsible for the higher average TOFs observed with HMOR. Besides, HZSM-5, which has the highest density of strong surface acid sites, showed the lowest TOF values of the series. Even more, HZSM-5 with a surface density of total and strong acid sites in the order of that of SiO$_2$–Al$_2$O$_3$, and also surface acid sites as strong as those of HMOR, showed TOF values even lower than that of the mesoporous solid acid. These results can be explained by considering diffusive limitations, as it was shown above. Slow diffusion of reactant and product molecules can be masking the intrinsic activity of acid sites on HZSM-5 under the experimental conditions used in this work, in contrast with the results previously reported for 1-phenylethanol dehydration [32].

The concentrations of the reactant and the product as a function of time for each catalyst are shown in Fig. 5. Both intramolecular and intermolecular dehydration took place over SiO$_2$–Al$_2$O$_3$ and thus both primary products, ENE and ETH, were formed from the very beginning. The initial ENE formation rate was about twice the initial formation rate of ETH. Therefore, taking into account the stoichiometric ratio, the initial selectivity to ENE over SiO$_2$–Al$_2$O$_3$ was only 45% (Table 4). The yield in ETH reached a maximum of about 11% and then diminished because it was slowly converted to HP. Instead, yield in ENE continued rising up to 46% (Fig. 5a). In order to get more information on the reactant and product evolutions, the overall selectivity (S_i), the local selectivity (S'_i), the carbon balance (%C), and the NOL conversion (X_{NOL}) were represented as a function of time in Fig. 6. It was observed that at the beginning of the reaction S'_{ENE} and S'_{ETH} were considerably lower than S_{ENE} and S_{ETH}, respectively (Fig. 6a and b). At high X_{NOL}, local selectivity approached the overall selectivity while %C increased, reaching

Fig. 4. Catalytic activity of acid solids in 1-indanol dehydration [p$_{N2}$ = 2 bar, T = 363 K, W_{CAT} = 0.25 g, C^0_{NOL} = 0.08 M, V_{SOLV} = 150 ml (cyclohexane), stirrer speed = 600 RPM].

Table 3
Catalytic performance of the acid solids used in the liquid-phase dehydration of 1-indanol [T = 363 K, p = 2 bar, W_{CAT} = 0.25 g, V_{SOLV} = 150 mL (cyclohexane), stirrer speed = 600 RPM].

Catalyst	r^0_{NOL}[a] (mol g^{-1} min^{-1})	r^0_{ENE}[b] (mol g^{-1} min^{-1})	TOF_{NOL}[c] (min^{-1})	TOF_{ENE}[d] (min^{-1})	Reaction time (min)	
					X_{NOL} = 0.5[e]	X_{NOL} = 0.9[f]
SiO$_2$–Al$_2$O$_3$	2.13×10^{-3}	9.58×10^{-4}	12.3	18.8	18.5	80.0
HBEA	6.75×10^{-3}	6.68×10^{-3}	23.8	45.1	2.5	6.0
HZSM-5	6.89×10^{-4}	6.82×10^{-4}	1.5	2.7	48.5	110.0
HMOR	2.84×10^{-3}	2.75×10^{-3}	55.7	59.8	7.0	16.0

[a] Initial conversion rate of 1-indanol (NOL).
[b] Initial formation rate of indene (ENE).
[c] Average turnover frequency (TOF) for NOL conversion considering the total acid site density determined by FTIR.
[d] Average turnover frequency (TOF) for ENE formation considering Brønsted acid site density determined by FTIR.
[e] Time necessary to reach a NOL conversion of 50%.
[f] Time necessary to reach a NOL conversion of 90%.

values higher than 90% (Fig. 6a and b). These differences between local and overall selectivities can be explained by considering that both ENE and ETH were retained on the SiO$_2$–Al$_2$O$_3$ surface due to the high interaction with the strongest acid sites and thus they diffused slowly to the liquid phase. Instead, HP did not interact with these acid sites and, once formed, they diffused rapidly to the liquid phase. As a consequence, no difference between S_{HP} and S'_{HP} was observed (Fig. 6b).

The carbon balance (%C) and selectivity (S_{ENE} and S'_{ENE}) as a function of time for zeolites are shown in Fig. 7a. In the case of HBEA, the main primary product observed in liquid phase was ENE with an initial selectivity of approximately 99% (Table 4), which remained almost constant even at 100% NOL conversion (Fig. 7a).

However, in spite of this high overall selectivity, the maximum ENE yield at 100% NOL conversion was only 54%. Besides, the ETH yield was lower than 1% and no HP formation was observed (Fig. 5b). As a consequence, over HBEA, the carbon balance at 100% NOL conversion reached only 55%, which indicates that an important amount of carbon-based compounds is retained inside the microporous structure of HBEA. In the first 10 min of reaction, X_{NOL} increased up to 100% and a large difference between S_{ENE} and S'_{ENE} was observed, whereas %C diminished and reached a minimum of approximately 40% at 100% NOL conversion. Afterwards, %C, η_{ENE} and S'_{ENE} increased with time until almost 55%, while S_{ENE} remained higher than 95%. These differences can be explained by assuming that NOL and/or ENE were converted to ETH or HP, which are bulky
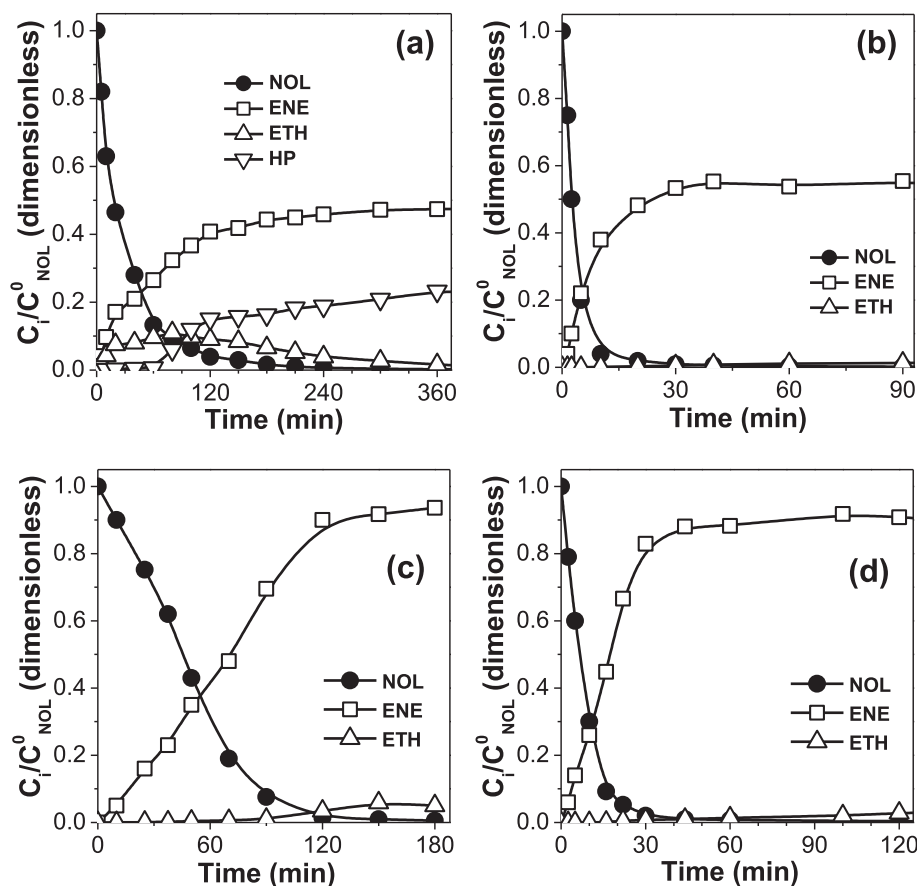
Fig. 5. Product and reactant dimensionless concentration profiles as a function of time for: (a) SiO$_2$–Al$_2$O$_3$, (b) HBEA, (c) HZSM-5, (d) HMOR [p_{N2} = 2 bar, T = 363 K, W_{CAT} = 0.25 g, C^0_{NOL} = 0.08 M, V_{SOLV} = 150 ml (cyclohexane), stirrer speed = 600 RPM].

Table 4
Catalytic performance of acid solids in liquid-phase dehydration of 1-indanol [T = 363 K, p = 2 bar, W_{CAT} = 0.25 g, V_{SOLV} = 150 mL (cyclohexane), stirrer speed = 600 RPM].

Catalyst	S^0_{ENE}[a] (%)	η_i (%)[b] (X_{NOL} = 90%)			η^F_{ENE}[c] (%)
		ENE	ETH	HP	
SiO$_2$–Al$_2$O$_3$	45	31	10	5	47
HBEA	99	46	0	0	54
HZSM-5	99	53	0	0	90
HMOR	97	61	1	0	94

[a] Initial selectivity to indene calculated as: $S^0_{ENE} = r^0_{ENE}/(r^0_{ENE} + 2 \cdot r^0_{ETH})$, where r^0_i is the initial formation rate of product i.
[b] Product yield at X_{NOL} = 90% (ENE: indene; ETH: ether; HP: heavy products).
[c] Maximum indene yield at the end of the run.

molecules that can be formed inside HBEA large cages but cannot diffuse through the HBEA microporous network. Only ENE molecules diffused through the micropores and reached liquid phase. It is worth mentioning that HBEA zeolite turned from white to light red or pink during the run. This change in color was observed in previous works and it was attributed to an important condensation of ENE to HP inside the HBEA cages [45,46]. These carbonaceous residues remained inside the cages of the spent catalyst even after extraction with dichloromethane. Thermogravimetric analysis (TGA) of these samples under O$_2$(20%)/He flow showed a weight loss of about 20 wt% between 300 and 500 °C, which could be
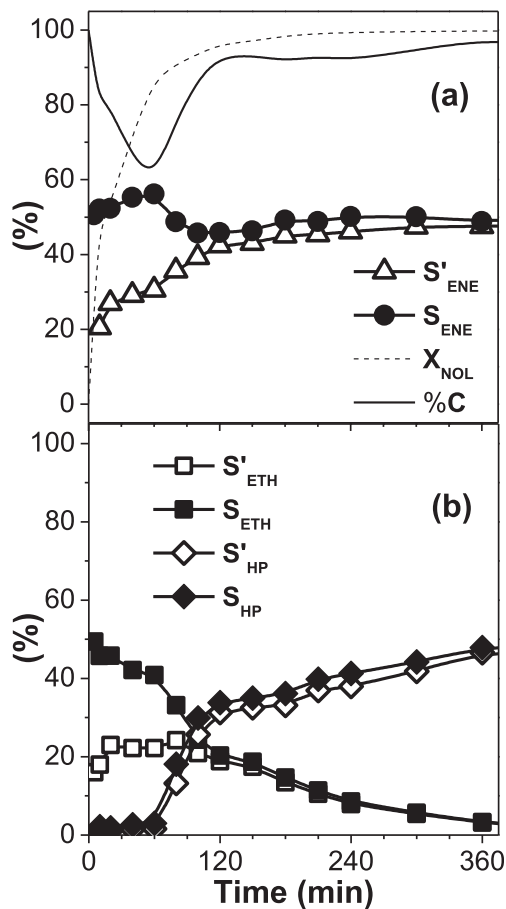
Fig. 6. Overall selectivity in liquid phase (S_i), local selectivity (S'_i), carbon balance (%C) and NOL conversion (X_{NOL}) as a function of time for SiO$_2$–Al$_2$O$_3$: (a) ENE (b) ETH and HP [p_{N2} = 2 bar, T = 363 K, W_{CAT} = 0.25 g, C^0_{NOL} = 0.08 M, V_{SOLV} = 150 ml (cyclohexane), stirrer speed = 600 RPM].
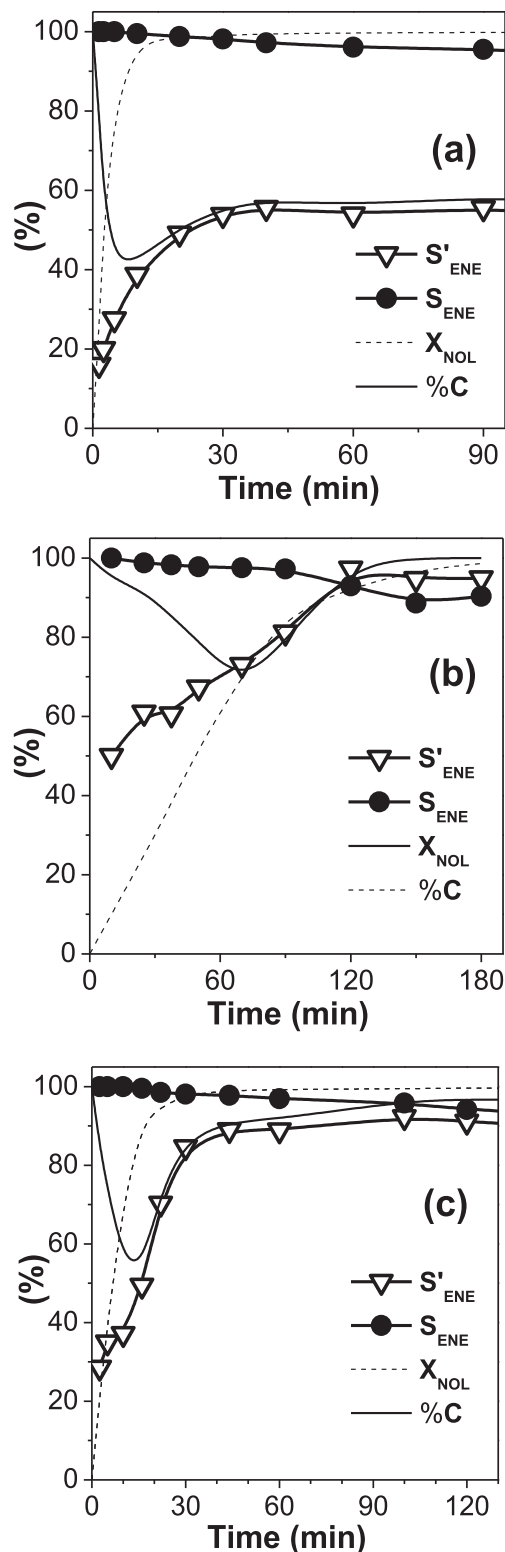
Fig. 7. Overall selectivity to indene (ENE) in liquid phase (S_{ENE}), local selectivity to ENE (S'_{ENE}), carbon balance (%C) and NOL conversion (X_{NOL}) as a function of time for: (a) HBEA, (b) HZSM-5, (c) HMOR [p_{N2} = 2 bar, T = 363 K, W_{CAT} = 0.25 g, C^0_{NOL} = 0.08 M, V_{SOLV} = 150 ml (cyclohexane), stirrer speed = 600 RPM].

attributed to the burn-out of the heavy compounds formed during the reaction [45,46].

With HZSM-5 zeolite, rapid ENE formation through intramolecular dehydration [47] and practically null ETH production

were observed at the beginning of the reaction, similarly to that observed with HBEA. Thus, the initial selectivity to ENE was 99%. The overall selectivity diminished slightly during the run, while S'_{ENE} increased with time up to above 90% (Fig. 7b). In agreement with this, the maximum η_{ENE} was around 90%, whereas the maximum yield in ETH was only about 5% and no detectable amounts of HP were observed (Fig. 5c and Table 4). S'_{ENE} increased with time until it became approximately close to S_{ENE}, whereas %C diminished up to 70% and then increased up to almost 100% at X_{NOL} higher than 90%. These results show that ENE was produced by selective intramolecular dehydration of NOL, and that NOL and ENE diffusion through the HZSM-5 microporous network was very slow.

Finally, a similar behavior was observed with HMOR zeolite: a very high initial selectivity to ENE ($S^0_{ENE} = 97\%$) that diminished slightly during the run, and an increase of η_{ENE} and S'_{ENE} with time up to 94% and 91%, respectively (Table 4, Figs. 5d and 7c). In this case, even after reaching 100% NOL conversion, the ENE yield continued to increase from 82 to 94%. The %C reached a minimum of 55% for a conversion of 80% and then increased up to almost 100%. These results show that, as for the case of HZSM-5, NOL and ENE diffuse very slowly through the microporous network of HMOR. It is worth noticing that over HZSM-5 and HMOR, the yield and local selectivity to ENE at $X_{NOL} > 90\%$ increased from 50–60% up to 90–95% with low or none production of ETH and HP (Figs. 5c–d and 7b–c, Table 4). These results would indicate that both molecular sieves, HZSM-5 and HMOR, are very selective for the intramolecular dehydration of NOL into ENE but slow diffusion of reactant and product molecules takes place inside their micropores. On the other hand, over HBEA, the yield and local selectivity to ENE increased just from 46% up to 54% even for $X_{NOL} > 90\%$ (Figs. 5b and 7a, Table 4). This would indicate that both reactant and product molecules also diffused very slowly, but in this case something else was formed and remained trapped inside HBEA microporous network.

In summary, all of the microporous samples used in this work are initially very selective for NOL intramolecular dehydration in liquid phase ($S^0_{ENE} \geq 97\%$, Table 4), in contrast with the mesoporous SiO$_2$–Al$_2$O$_3$ sample ($S^0_{ENE} = 45\%$, Table 4). Furthermore, small amounts of HP in the liquid phase were detected during reaction with the three zeolites, whereas an HP yield of about 20% was obtained with SiO$_2$–Al$_2$O$_3$. These results indicate that shape selectivity plays a very important role for favoring the intramolecular dehydration of NOL into ENE. Final ENE yields higher than 90% were reached with HZSM-5 and HMOR. In contrast, a final ENE yield of only 54% at $X_{NOL} = 100\%$ could be obtained with HBEA, while an important lack of carbon balance was determined. This was attributed to the formation of ETH and HP inside large HBEA cages, which cannot diffuse through the HBEA micropores.

Taking into account that the microporous structure seems to be crucial to explain the catalytic performance of the acid solids used in this work, and to get more evidence about the correlation between catalytic activity and textural properties of the solids, the micropore diameter of each zeolite was compared with the molecular sizes and kinetic diameters of the reactant and product compounds (Table 5). It is well known that three different types of shape selectivities can occurred in zeolites: product, reactant and transition state selectivity, which can direct a catalytic reaction avoiding undesirable side reactions [48–51].

The low selectivity to ENE obtained with SiO$_2$–Al$_2$O$_3$ (Fig. 6a) can be explained on the basis of the high total density of acid sites, mainly Lewis type (Table 2), and the mesoporous structure (Table 1). In a previous work dealing with the dehydration of 1-phenylethanol in liquid phase, it was proposed that the high density of acid sites and the high ratio L/(L + B) promote ether formation [46]. Besides, it is clear that there are no restrictions inside

the mesopores of SiO$_2$–Al$_2$O$_3$ for the formation of surface intermediates that give place to bulky molecules as ETH and HP (Tables 1 and 5). In addition, high surface density of acid sites, mainly Lewis type, favors the interaction between neighboring adsorbed reactant molecules to give ETH and HP from NOL and ENE [47], which can diffuse outside the mesopores to the liquid phase (Fig. 5a).
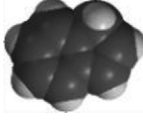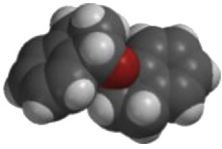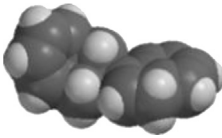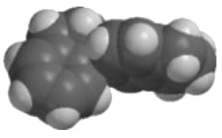
Over HBEA, with surface acid sites of varying strength and L/(L + B) = 0.48 (Table 2), the intramolecular alcohol dehydration was initially favored [45]. Although the initial and overall selectivity to ENE were very high, S'_{ENE} only reached 55% at the end of reaction (Fig. 7a). This is in agreement with a final η_{ENE} of only 54% and a 45% of the carbon atoms missing at $X_{NOL} = 100\%$. From the analysis of Tables 1 and 5, it is clear that ENE can be formed and diffuse within the 12-member ring channels of HBEA but ETH and HP cannot be formed inside these micropores. The main reason could be that the surface transition states necessary to produced ETH and HP are too bulky to fit inside this type of micropores. However, some authors have reported the presence of cavities of about 12 Å in the channel intersections of HBEA [52,53], where bulky transition states leading to ETH and HPs can be accommodated. These byproducts can be formed inside those large cavities but they are not able to diffuse outside because their kinetic diameters (Table 5) are larger than the micropore size of HBEA (Table 1). As these bulky molecules are not able to diffuse to the liquid phase, the high overall selectivity and the missing 45% in the C balance can be explained on the basis of the product shape selectivity, in agreement with results obtained in previous works [45,46].

In the case of HZSM-5, with a high acid site density and similar proportion of Lewis and Brønsted acid sites, i.e. L/(L + B) = 0.45, the initial selectivity to ENE was similar to HBEA (Table 4). However, unlike HBEA, S_{ENE} and S'_{ENE} became similar and approximately equal to 90% after 2 h reaction, at $X_{NOL} = 100\%$, with the carbon balance closing in 95% (Fig. 7b). As a consequence, the final ENE yield was almost 90% (Table 4), i.e. a much higher yield than that obtained with HBEA. HZSM-5 does not have large cages in its microporous structure so bulky compounds cannot be formed. This is in agreement with the high yield in ENE reached with this zeolite. On the other hand, with HMOR, which has a low surface density of acid sites and a high ratio of Brønsted to Lewis sites, initial (S^0_{ENE}) and overall selectivity to ENE (S_{ENE}) higher than 94% were obtained. In this case, S'_{ENE} approached S_{ENE} after 100 min of reaction (Fig. 7c), a time longer than needed to reach 100% NOL conversion. At this time, the maximum ENE yield with HMOR, i.e. 94%, was reached (Table 4).

Catalytic performance of both HZSM-5 and HMOR cannot be explained by only considering solid acidity. It was concluded from data in Tables 1 and 5 that both NOL and ENE can be accommodated inside microporous network of both HZSM-5 and HMOR. The experimental results indicate that ENE diffuses slowly outside the microporous network in both zeolites (Table 4 and Fig. 5). However, the kinetic diameters of NOL and ENE (Table 5) are larger than the size usually reported for HZSM-5 micropores (Table 1). In spite of this, it is concluded from the catalytic results that NOL diffused throughout HZSM-5 micropores and reacted to give ENE, which in turn diffused slowly to the liquid phase (Fig. 5c). Other authors have proposed that if Norman radii for Si and O atoms are used, then values up to 0.7 Å larger can be estimated for the micropore diameters [54]. Considering this correction, NOL and ENE could diffuse through the HZSM-5 micropores and catalytic results could be explained. In summary, NOL diffusion, intramolecular dehydration of NOL into ENE and finally ENE diffusion throughout microporous network would be possible with both HMOR and HZSM-5. On the other hand, neither HMOR nor HZSM-5 has large cavities in their microporous network. Besides, surface acid sites on

Table 5
Molecular structure and molecule size of the reactant and reaction products.

Compound[a]	Optimized 3D structure[b]	E[c] (kJ mol^{-1})	CD[d] (Å)	CL[e] (Å)	KD[f] (Å)
NOL		100.78	5.00	6.67	6.21
ENE		115.96	5.00	6.73	5.93
ETH		257.94	5.92	11.30	7.63
HP1		576.72	5.87	11.67	7.45
HP2		543.84	6.68	11.44	7.45

[a] NOL: 1-indanol; ENE: indene; ETH; di-1-indanyl ether; HP1: 2-(2′3′-dihydro-1′H-inden-1′-yl)-1H-indene; HP2: 6-(2′,3′-dihydro-1′H-inden-1′-yl)-1H-indene.
[b] Determined using molecular modeling as described in Experimental section.
[c] Energy of optimized molecule.
[d] Critical diameter.
[e] Critical length.
[f] Estimated kinetic diameter [35,36].

HMOR are probably isolated from each other due to the low acid density. Therefore, it is expected that intermolecular dehydration of NOL into ETH over HMOR might occur mainly through an Eley-Rideal-type mechanism [47]. However, HMOR micropores are not large enough as to allow the formation of the bulky surface transition state necessary to convert NOL into ETH via this mechanism. Thus, the restricted transition state selectivity explains the very high S^0_{ENE} observed with HMOR. Also the low density of surface acid sites reduces the probability of interaction between ENE molecules adsorbed on neighboring sites and so hampers the production of HP from ENE. Then, the most likely reaction mechanism on HMOR is tintramolecular dehydration of NOL into ENE with high final yields (η_{ENE} = 94%). On the contrary, chemisorption of two NOL molecules on two neighboring acid sites of HZSM-5 surface is highly probable. However, as ETH has a kinetic diameter of around 7.6 Å (Table 5), if ETH is formed, its diffusion through the zeolite micropores is restricted and it would be slowly dehydrated into ENE. This can also be a reason for the slow increase of ENE yield with time observed for HZSM-5. The slow diffusion of ENE molecules in HZSM-5 and HMOR from the microporous network to the liquid phase can be explained on the basis of a combined effect of strong surface acid sites and large kinetic diameter of reactant and product molecules. The low amount of ETH ($\eta_{ETH} \cong 5\%$) observed for HZSM-5 and HMOR can be due to the contribution of weak acid sites located on the external surface of the zeolite particles, with an acid strength similar to that of silanols on SiO$_2$–Al$_2$O$_3$ [55].

In summary, it is concluded that transition state shape selectivity and diffusional restrictions are crucial to reach very high yield and selectivity to ENE in the liquid-phase NOL dehydration, which shows the important role that the microporous structure plays in this reaction. The pattern found in this work for mass transfer limitations within the micropores would be: HZSM-5 > HMOR > HBEA, in agreement with the increase of the ratio between molecular and pore dimensions. Strong acid sites on the catalyst surface are also playing an important role in retarding the diffusion of ENE molecules.

4. Conclusions

The selective liquid-phase dehydration of 1-indanol to indene was successfully carried out over HMOR (dealuminated mordenite) and HZSM-5 zeolites, reaching indene yields higher than 90%. Indene molecules are very stable on these zeolites and they are not converted into bulky or heavy compounds. The high selectivity to indene observed with these catalysts depended on a combination of acid properties and microporous structures. The formation of bulky surface intermediates, which lead to undesirable by-products, can be hampered by transition state shape selectivity and diffusional restrictions using zeolites with the adequate channel size. Then, the micropore size becomes a very important parameter to favor the selective intramolecular dehydration of 1-indanol to indene over the intermolecular dehydration of 1-indanol and the bimolecular condensation of indene into heavy products. Besides, HMOR was more active than HZSM-5 probably due to an easier accessibility of NOL to the strongest surface acid sites.

The results obtained in this work reveal that this catalytic reaction can be used in a one-pot hydrogenation/dehydration

process. This novel process could replace the traditional industrial one and so avoid the use of toxic raw materials and complex unit operations to obtain indene.

Acknowledgments

References

[1] Y. Gao, Y. Hong, X. Nie, R.P. Bakale, R.R. Feinberg, C.M. Zepp, US Patent 5599985 (1997), Sepracor, Inc.
[2] X.M. O'Brien, J.A. Parker, P.A. Lessard, A.J. Sinskey, Appl. Microbiol. Biotechnol. 59 (2002) 389–399.
[3] H. Sato, M. Makino, US Patent 4946915 (1990); Nippon Oil Company Ltd.
[4] Y. Yamashita, S. Iwata, T. Yamanaka, A. Yoshida, K. Ushikubo, US Patent 6900273 (2005); Hitachi Chemical Co., Ltd.
[5] R.N. Austin, T.J. Clark, T.E. Dickson, C.M. Killian, T.A. Nile, D.J. Schabacker, A.T. McPhail, J. Organomet. Chem. 491 (1995) 11–18.
[6] H.G. Alt, A. Koppl, Chem. Rev. 100 (2000) 1205–1221.
[7] J. Yang, M.V. Lakshmikantham, M.P. Cava, D. Lorcy, J.R. Bethelot, J. Org. Chem. 65 (2000) 6739–6742.
[8] L. Kahl, US Patent 1943078 (1934).
[9] Y. Takigawa, H. Nakaoka, US Patent 6291735 (2001), ADCHEMCO Corporation.
[10] K. Sakuma, K. Shiotani, H. Ishida, JP Patent 60-87230A (1985), Nippon Steel Chem. Co.
[11] H. Mori, Y. Sugio, US Patent 6818121 (2004), JFE Chemical Corporation.
[12] J.C. Montagna, R.D. Galli, J. Freel, US Patent 4280881 1981, Gulf Research & Development Company.
[13] E.J. Hoffmann, B. Souby, A.M. Souby, US Patent 27636701 (1956), Esso Research and Engineering Company.
[14] J.P. Bartek, R.K. Grasselli, US Patent 4143082 (1979), The Standard Oil Company.
[15] O.A. Kiikka, G.S. Li, US Patent 4291181 (1981), Standard Oil Company.
[16] J.P. Bartek, R.L. Cepulis, R.K. Grasselli, US Patent 4292455 (1981), The Standard Oil Company.
[17] Y. Matsumura, US Patent 6380450 (2002), Nippon Petrochemicals Company.
[18] S.E. Pedersen, W.G. Shaw, L.L. Pfingsten, US Patent 4613711 (1986), The Standard Oil Company.
[19] W.E. Elwell, US Patent 2531328 (1950), California Research Corporation.
[20] J.D. Burrington, R.K. Grasselli, C.T. Kartisek, US Patent 4374293 (1983), The Standard Oil Co.
[21] J. Weiguny, H. Borchert, U. Dingerdissen, US Patent 5789593 (1998), Targar GmbH.
[22] R. Roesky, J. Weiguny, H. Bestgen, U. Dingerdissen, Appl. Catal. A: Gen. 176 (1999) 213–220.
[23] P.L. Kuch, D.R. Herrington, US Patent 4255601 (1981), The Standard Oil Company.
[24] N.M. Bertero, C.R. Apesteguía, A.J. Marchi, Catal. Today 172 (2011) 171–176.
[25] N.M. Bertero, C.R. Apesteguía, A.J. Marchi, in: Proceedings of the X EuropaCat, August 2011. Glasgow, Scotland.

[26] A. Tarlani, A. Riahi, M. Abedini, M.M. Amini, J. Muzart, J. Mol. Catal. A: Chem. 260 (2006) 187–189.
[27] E. Alesso, R. Torviso, L. Finkielsztein, B. Lantaño, G. Moltrasio, J. Aguirre, P. Vázquez, L. Pizzio, C. Cáceres, M. Blanco, H. Thomas, J. Chem. Res. (S) (2001) 508–510.
[28] J.B. Parra, J.C. de Sousa, R.C. Bansal, J.J. Pis, J.A. Pajares, Ads. Sci. Technol. 12 (1995) 51–66.
[29] J.B. Parra, C.O. Ania, A. Arenillas, J.J. Pis, Stud. Surf. Sci. Catal. 144 (2002) 537–543.
[30] B.C. Lippens, B.G. Linsen, J.H. De Boer, J. Catal. 3 (1964) 32–37.
[31] W.D. Harkins, G. Jura, J. Chem. Phys. 11 (1943) 431–432.
[32] N.M. Bertero, C.R. Apesteguía, A.J. Marchi, Catal. Commun. 10 (2009) 1339–1344.
[33] A.D. Becke, J. Chem. Phys. 98 (1993) 5648–5652.
[34] M.J. Frisch, G.W. Trucks, H.B. Schlegel, G.E. Scuseria, M.A. Robb, J.R. Cheeseman, J.J.A. Montgomery, T. Vreven, K.N. Kudin, J.C. Burant, J.M. Millam, S.S. Iyengar, J. Tomasi, V. Barone, B. Mennucci, M. Cossi, G. Scalmani, N. Rega, G.A. Petersson, H. Nakatsuji, M. Hada, M. Ehara, K. Toyota, R. Fukuda, J. Hasegawa, T. Nakajima, Y. Honda, O. Kitao, H. Nakai, M. Klene, X. Li, J.E. Knox, H.P. Hratchian, J.B. Cross, V. Bakken, C. Adamo, J. Jaramillo, R. Gomperts, R.E. Stratmann, O. Yazyev, A.J. Austin, R. Cammi, C. Pomelli, J.W. Ochterski, P.Y. Ayala, K. Morokuma, G.A. Voth, P. Salvador, J.J. Dannenberg, V.G. Zakrzewski, S. Dapprich, A.D. Daniels, M.C. Strain, O. Farkas, D.K. Malick, A.D. Rabuck, K. Raghavachari, J.B. Foresman, J.V. Ortiz, Q. Cui, A.G. Baboul, S. Clifford, J. Cioslowski, B.B. Stefanov, G. Liu, A. Liashenko, P. Piskorz, I. Komaromi, R.L. Martin, D.J. Fox, T. Keith, M.A. Al-Laham, C.Y. Peng, A. Nanayakkara, M. Challacombe, P.M.W. Gill, B. Johnson, W. Chen, M.W. Wong, C. Gonzalez, J.A. Pople, Gaussian '03, Gaussian, Inc., Wallingford, CT, 2004.
[35] R.B. Bird, W.E. Stewart, E.N. Lighfoot, Transport Phenomena, John Wiley & Sons, New York, 1960, p. 26.
[36] H. Wang, M. Frenklach, Combust. Flame 96 (1994) 163–170.
[37] E.J.M. Hensen, D.G. Poduval, P.C.M.M. Magusin, A.E. Coumans, J.A.R. van Veen, J. Catal. 269 (2010) 201–218.
[38] Y. Miyamoto, N. Katada, M. Niwa, Micropor. Mesopor. Mater. 40 (2000) 271–281.
[39] N.M. Bertero, C.R. Apesteguía, A.J. Marchi, Catal. Commun. 10 (2008) 261–265.
[40] G. Busca, Catal. Today 41 (1998) 191–206.
[41] C.A. Emeis, J. Catal. 141 (1993) 347–354.
[42] J. Wang, L. Huang, H. Chen, Q. Li, Catal. Lett. 55 (1998) 157–163.
[43] P.A. Ramachandran, R.V. Chaudhari, Three Phase Catalytic Reactors, Gordon and Breach, New York, 1983.
[44] A.J. Marchi, G.F. Froment, Appl. Catal. A: Gen. 94 (1993) 91–106.
[45] S. Wuyts, K. De Temmerman, D.E. de Vos, P.A. Jacobs, Chem. Eur. J. 11 (2005) 386–397.
[46] K. Pitchumani, V. Ramamurthy, Chem. Commun. (1996) 2763–2764.
[47] N.M. Bertero, A.F. Trasarti, C.R. Apesteguía, A.J. Marchi, Appl. Catal. A: Gen. 458 (2013) 28–38.
[48] A. Corma, Chem. Rev. 97 (1997) 2373–2419.
[49] L.A. Clark, M. Sierka, J. Sauer, J. Am. Chem. Soc. 126 (2004) 936–947.
[50] B. Smit, T.L.M. Maesen, Nature 451 (2008) 671–678.
[51] J. Huang, Y. Jiang, V.R.R. Marthala, M. Hunger, J. Am. Chem. Soc. 130 (2008) 12642–12644.
[52] Z. Da, Z. Han, P. Magnoux, M. Guisnet, Appl. Catal. A: Gen. 219 (2001) 45–52.
[53] R. Benslama, J. Fraissard, A. Albizane, F. Fajula, F. Figueras, Zeolites 8 (1988) 196–198.
[54] M. Cook, W.C. Conner, in: Proceedings of the International Zeolite Conference, 12th, Baltimore, July 5-10, 1998, p. 409.
[55] M. Trombetta, T. Armaroli, A.G. Alejandre, J. Ramirez Solis, G. Busca, Appl. Catal. A: Gen. 192 (2000) 125–136.
[56] http://www.iza-online.org.